# Elastic Least-Squares Reverse Time Migration Using Decoupled P- and S-Wave Equations for PP and PS Reflectivity Imaging

Xuejian Liu and Lianjie Huang

***Abstract*— Recent development of elastic least-squares reverse time migration (ELSRTM) focuses on producing high-resolution images of elastic model perturbations such as elastic impedance images. There is a clear gap between such development and conventional elastic reverse time migration (ERTM) that generates images of PP and PS reflectors. We develop a novel ELSRTM method for iteratively enhancing PP and PS images. To achieve this purpose, we introduce a vector reflection demigration operator by combining reflection demigration theory with decoupled velocity–stress equations. This vector ELSRTM (VELSRTM) method is practical without introducing any phase distortions of sources, adjoint, or demigration wavefields and performs well with kinematically accurate migration velocity models. We demonstrate the effectiveness and advantages of our VELSRTM method using layer, Marmousi2, SEG Advanced Modeling (SEAM) models, and a field data example. Numerical results show that our VELSRTM method with only a few iterations successfully improves both PP and PS images with higher spatial resolution and more balanced imaging amplitudes than ERTM images.**

***Index Terms*— Elastic, least-squares, reflectivity imaging, reverse time migration (RTM), vector demigration, vector elastic least-squares reverse time migration (VELSRTM).**

## I. Introduction

REVERSE time migration (RTM) is a routine procedure of seismic processing for imaging complex subsurface structure [1]. However, although the Earth is elastic (Fig. 1), most RTM methods are limited to the acoustic assumption. With improving computational capacity and seismic data acquisition techniques, elastic RTM (ERTM) methods are increasingly used to handle three-component (3C) seismic data to better image subsurface [2]. ERTM can produce not only conventional PP images but also converted PS images [3], [4], [5], [6], [7]. Joint analysis of PP and PS images can help detect sweet spots of tight-sandstone reservoirs and interpret reflectors within or beneath gas-charged sediments [2].

Manuscript received 16 April 2023; revised 14 August 2023 and 19 September 2023; accepted 18 October 2023. Date of publication 23 October 2023; date of current version 17 November 2023. This work was supported by the U.S. Department of Energy (DOE) through the Los Alamos National Laboratory (LANL), which is operated by Triad National Security, LLC, for the National Nuclear Security Administration (NNSA) of U.S. DOE, under Contract 89233218CNA000001. *(Corresponding authors: Xuejian Liu; Lianjie Huang.)*

The authors are with the Los Alamos National Laboratory, Los Alamos, NM 87545 USA (e-mail: xuejianliu17@gmail.com; ljh@lanl.gov).

Digital Object Identifier 10.1109/TGRS.2023.3326739

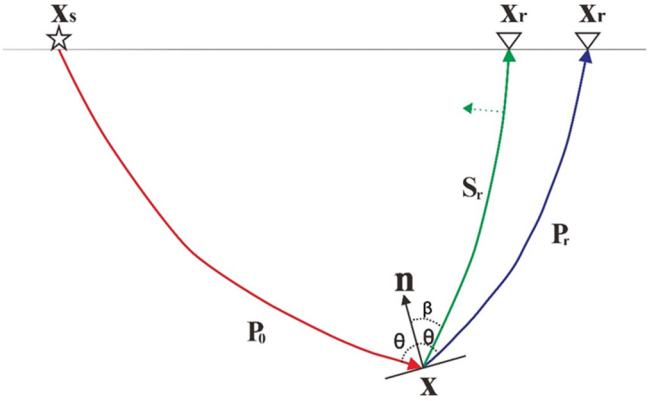


Fig. 1. Schematic illustration of seismic reflections in isotropic elastic media. The red, blue, and green arrow lines, respectively, represent the downgoing P-wave, the reflected P-wave (i.e., PP wave), and the converted S-wave (i.e., PS wave). The polarization direction of P-wave is along with its propagation direction, whereas the polarization direction of S-wave is perpendicular to its propagation direction as indicated by the green dashed-line arrow.

ERTM can be straightforwardly implemented by cross-correlating P- and S-wavefields, which are computed by applying the divergence and curl operations to elastic vector wavefields, respectively. However, this method produces prestack PS images with polarity reversal, which is hard to be accurately accounted for, leading to destructive stacking [3]. By contrast, vector ERTM (VERTM) can be implemented more easily because it does not have the polarity reversal issue on the converted PS images, which are produced by applying the dot-product imaging condition to independently propagated vector P- and S-waves through decoupled elastic-wave equations [4], [5], [6], [7], [8]. Additionally, the decoupling procedure does not distort the phase characteristics of P- and S-waves [9].

However, ERTM belongs to standard migration rather than reflectivity inversion, which tends to suffer from low imaging resolution, unbalanced imaging amplitudes, and migration artifacts [10], [11], [12]. Least-squares migration (LSM) is a linear inversion, and it can mitigate these issues and improve the subsurface imaging quality [13], [14], [15], [16], [17], [18], [19]. Elastic least-squares RTM (ELSRTM) combines LSM with elastic Born modeling. However, ELSRTM usually produces images of elastic model perturbations, such as elastic moduli, velocity, or impedance perturbations based on parameterization choices [20], [21], [22], [23], which are different from PP and PS images produced using ERTM.

An alternative ELSRTM method employs the energy norm [24], which, however, only produces a scalar reflectivity image with multicomponent data.

To be consistent with ERTM for PP and PS imaging, we develop a new vector ELSRTM (VELSRTM) method using a novel vector reflection demigration operator based on the nature of the reflectivity function. We extend the reflection demigration formula for acoustic media [25], [26], to the vector case for modeling PP and PS reflections [27]. We compute gradients using VERTM with updated adjoint sources at each iteration. We derive demigration and migration formulas in the time domain using decoupled velocity–stress wave equations. We demonstrate using synthetic and field seismic data that our new imaging method successfully improves PP and PS images with higher spatial resolution and more balanced imaging amplitudes.

## II. Theory

### A. Decoupled P- and S-Wave Equation

In isotropic elastic media, $\mathbf{U} = (u_x, u_y, u_z)^{\mathrm{T}}$ represents the vector displacement wavefield with $x$, $y$, and $z$ components, $\lambda$ and $\mu$ denote Lamé moduli, $\rho$ denotes the density, and spatial-domain mathematical operators $\nabla\times$, $\nabla\cdot$, and $\nabla$, respectively, represent the curl, divergence, and gradient calculation. Under the assumption of locally smoothed shear modulus $\mu$ as shown in Appendix A, we can define decoupled elastic-wave equations as follows:

$$\rho\frac{\partial^2\mathbf{U}^{\mathrm{p}}}{\partial t^2} = \nabla(\lambda+2\mu)\nabla\cdot\mathbf{U} \tag{1a}$$

$$\rho\frac{\partial^2\mathbf{U}^{\mathrm{s}}}{\partial t^2} = -\nabla\times\mu\nabla\times\mathbf{U} \tag{1b}$$

$$\mathbf{U} = \mathbf{U}^{\mathrm{p}} + \mathbf{U}^{\mathrm{s}} \tag{1c}$$

where superscripts denote P- and S-wave modes.

To reduce numerical dispersion caused by low S-wave velocities, decoupled velocity–stress equations are preferred [4], [9]. In the 2-D case, the decoupled P-wave equation is rewritten as

$$\begin{cases} \rho\dfrac{\partial v_x^{\mathrm{p}}}{\partial t} = \dfrac{\partial}{\partial x}\dfrac{(\lambda+2\mu)}{2(\lambda+\mu)}(\sigma_{xx}+\sigma_{zz}) \\ \rho\dfrac{\partial v_z^{\mathrm{p}}}{\partial t} = \dfrac{\partial}{\partial z}\dfrac{(\lambda+2\mu)}{2(\lambda+\mu)}(\sigma_{xx}+\sigma_{zz}). \end{cases} \tag{2a}$$

Then, we can produce the decoupled S-wave as

$$\begin{cases} v_x^{\mathrm{s}} = v_x - v_x^{\mathrm{p}} \\ v_z^{\mathrm{s}} = v_z - v_z^{\mathrm{p}} \end{cases} \tag{2b}$$

where $\sigma_{xx}$ and $\sigma_{zz}$, respectively, represent horizontal and vertical normal stress, and $v_x$ and $v_z$, respectively, represent horizontal and vertical particle-velocity components.

Another format of the decoupled velocity–stress formula can be derived by directly splitting constitutive relations, which is equivalent to (1), as shown in Appendix B. We develop the VELSRTM method based on these two types of decoupled velocity–stress equations.

### B. VELSRTM for PP and PS Reflectivity Imaging

The VELSRTM method minimizes the $L_2$ misfit $f(\mathbf{R})$

$$f(\mathbf{R}) = \frac{1}{2}\|\mathbf{L}\mathbf{R} - \mathbf{D}_{\mathrm{obs}}\|^2 \tag{3}$$

where observed data $\mathbf{D}_{\mathrm{obs}} = \begin{bmatrix}\mathbf{D}_x \\ \mathbf{D}_z\end{bmatrix}$ at receiver positions contain PP and converted PS wave modes in most cases where P-wave dominant sources are excited, and the modeling operator $\mathbf{L}$ and the reflectivity model $\mathbf{R}$ are, respectively, defined as $\mathbf{L} = [\mathbf{L}^{\mathrm{pp}}\ \mathbf{L}^{\mathrm{ps}}]$ and $\mathbf{R} = \begin{bmatrix}\mathbf{R}_{\mathrm{pp}} \\ \mathbf{R}_{\mathrm{ps}}\end{bmatrix}$.

The corresponding gradient is written as

$$\boldsymbol{g} = \frac{\partial f(\mathbf{R})}{\partial \mathbf{R}} = \mathbf{L}^{\mathrm{T}}(\mathbf{L}\mathbf{R} - \mathbf{D}_{\mathrm{obs}}) \tag{4}$$

where $\mathbf{L}^{\mathrm{T}}$ represents the adjoint migration operator. The gradient at the first iteration can be regarded as VERTM for PP and PS images. For simplicity, a gradient descent algorithm

$$\mathbf{R}^{(i+1)} = \mathbf{R}^{(i)} - \lambda^{(i)}\boldsymbol{g}^{(i)} \tag{5}$$

is used to represent the iterative procedure to seek the solution minimizing the misfit function in (3), where $i$ represents the iteration number and $\lambda$ represents the step length. In real applications, we use a preconditioned conjugate algorithm to achieve better convergence.

To implement the modeling procedure $\mathbf{L}\mathbf{R}$ at each iteration, we develop a vector demigration operator extending from the concept originally used in acoustic imaging as shown in Appendix C. Extending reflection demigration equations for acoustic media [25], [26], we compactly describe the demigration operator for modeling vector PP and PS reflection waves [27] at each time step as

$$\begin{cases} \mathbf{V}_{\mathrm{r}}^{\mathrm{p}} = \mathbf{M}_{\mathrm{p}}\left(\mathbf{R}_{\mathrm{pp}}\dfrac{\partial}{\partial t}\mathbf{V}_0^{\mathrm{p}}\right) \\ \mathbf{V}_{\mathrm{r}}^{\mathrm{s}} = \mathbf{M}_{\mathrm{s}}\left(\mathbf{R}_{\mathrm{ps}}\dfrac{\partial}{\partial t}\mathbf{V}_0^{\mathrm{p}}\right) \end{cases} \tag{6}$$

where $\mathbf{M}_{\mathrm{p}}$ and $\mathbf{M}_{\mathrm{s}}$ indicate the forward-modeling operators, and $\mathbf{V}_0^{\mathrm{p}}$, $\mathbf{V}_{\mathrm{r}}^{\mathrm{p}}$, and $\mathbf{V}_{\mathrm{r}}^{\mathrm{s}}$ represent the P-wave vector of source wavefields, the P-wave vector of receiver wavefields, and the S-wave vector of receiver wavefields, respectively. The separately modeled PP and PS vector waves can be summed together to form multicomponent modeled data $\mathbf{D}_{\mathrm{mod}} = \begin{bmatrix}\mathbf{d}_x \\ \mathbf{d}_z\end{bmatrix}$.

Correspondingly, at each iteration, the adjoint imaging condition for gradient [26], [27] can be compactly written as

$$\begin{cases} \tilde{R}_{\mathrm{pp}}(\mathbf{x}) = -\displaystyle\int\int \mathbf{V}_0^{\mathrm{p}}\cdot\frac{\partial}{\partial t}\tilde{\mathbf{V}}_{\mathrm{r}}^{\mathrm{p}}\mathrm{d}t\,\mathrm{d}\mathbf{x}_{\mathrm{s}} \\ \tilde{R}_{\mathrm{ps}}(\mathbf{x}) = -\displaystyle\int\int \mathbf{V}_0^{\mathrm{p}}\cdot\frac{\partial}{\partial t}\tilde{\mathbf{V}}_{\mathrm{r}}^{\mathrm{s}}\mathrm{d}t\,\mathrm{d}\mathbf{x}_{\mathrm{s}} \end{cases} \tag{7}$$

where $\tilde{\mathbf{V}}_{\mathrm{r}}^{\mathrm{p}}$ and $\tilde{\mathbf{V}}_{\mathrm{r}}^{\mathrm{s}}$ indicate the receiver P- and S-wavefields, respectively, and $\tilde{R}_{\mathrm{pp}}(\mathbf{x})$ and $\tilde{R}_{\mathrm{ps}}(\mathbf{x})$ indicate the PP and PS images, respectively. Here, the time-domain operator $-\partial/(\partial t)$ corresponds to the operation of $-i\omega$ in the frequency domain, as shown in Appendix C.

Furthermore, in Sections II-C and II-D, we give detailed velocity–stress equations for demigration and migration operations.

### C. Vector Demigration for Modeling PP and PS Reflections With Velocity–Stress Formulas

To numerically implement the vector reflection demigration formulas in (6), we need to solve the pure P-wave at the source side and the pure P- and S-waves at the receiver side, which involves solving three decoupled elastic-wave equations. The procedure makes the vector demigration very expensive and the VELSRTM is not computationally practical. Nevertheless, for smoothed migration velocity models, we can simplify the velocity–stress formulas in (B-4)–(B-6) to efficiently simulate the pure P- and S-waves.

On the other hand, we need to establish subsurface virtual sources as $R_{\rm pp}(\mathbf{x})\partial/(\partial t)\mathbf{V}_0^{\rm p}$ and $R_{\rm ps}(\mathbf{x})\partial/(\partial t)\mathbf{V}_0^{\rm p}$ to simulate PP- and PS-waves based on (6). Comparing (A-3) with (A-4)–(A-6) indicates that the time derivative can be implicitly applied to the source term when we solve the velocity–stress equations. For example, if we employ the virtual source term of $R_{\rm pp}(\mathbf{x})\partial/(\partial t)v_x^{\rm p}$, the source is set as $R_{\rm pp}(\mathbf{x})v_x^{\rm p}$ in the first-order velocity–stress equations. Then, we simulate the vector PP and converted PS reflection waves by solving the following equations:

$$\begin{cases} \rho_0\dfrac{\partial v_{0x}^{\rm p}}{\partial t} = \dfrac{\partial \sigma_0^{\rm p}}{\partial x} \\ \rho_0\dfrac{\partial v_{0z}^{\rm p}}{\partial t} = \dfrac{\partial \sigma_0^{\rm p}}{\partial z} \\ \dfrac{\partial \sigma_0^{\rm p}}{\partial t} = (\lambda_0+2\mu_0)\left(\dfrac{\partial v_{0x}^{\rm p}}{\partial x}+\dfrac{\partial v_{0z}^{\rm p}}{\partial z}\right)+f \end{cases} \tag{8a}$$

$$\begin{cases} \rho_0\dfrac{\partial v_{rx}^{\rm p}}{\partial t} = \dfrac{\partial \sigma_{\rm r}^{\rm p}}{\partial x}+R_{\rm pp}(\mathbf{x})v_{0x}^{\rm p} \\ \rho_0\dfrac{\partial v_{rz}^{\rm p}}{\partial t} = \dfrac{\partial \sigma_{\rm r}^{\rm p}}{\partial z}+R_{\rm pp}(\mathbf{x})v_{0z}^{\rm p} \\ \dfrac{\partial \sigma_{\rm r}^{\rm p}}{\partial t} = (\lambda_0+2\mu_0)\left(\dfrac{\partial v_{rx}^{\rm p}}{\partial x}+\dfrac{\partial v_{rz}^{\rm p}}{\partial z}\right) \end{cases} \tag{8b}$$

and

$$\begin{cases} \rho_0\dfrac{\partial v_{rx}^{\rm s}}{\partial t} = \dfrac{\partial \sigma_{rxx}^{\rm s}}{\partial x}+\dfrac{\partial \sigma_{rxz}^{\rm s}}{\partial z}+R_{\rm ps}(\mathbf{x})v_{0x}^{\rm p} \\ \rho_0\dfrac{\partial v_{rz}^{\rm s}}{\partial t} = \dfrac{\partial \sigma_{rxz}^{\rm s}}{\partial x}+\dfrac{\partial \sigma_{rzz}^{\rm s}}{\partial z}+R_{\rm ps}(\mathbf{x})v_{0z}^{\rm p} \\ \dfrac{\partial \sigma_{rxx}^{\rm s}}{\partial t} = -2\mu_0\dfrac{\partial v_{rz}^{\rm s}}{\partial z} \\ \dfrac{\partial \sigma_{rzz}^{\rm s}}{\partial t} = -2\mu_0\dfrac{\partial v_{rx}^{\rm s}}{\partial x} \\ \dfrac{\partial \sigma_{rxz}^{\rm s}}{\partial t} = \mu_0\left(\dfrac{\partial v_{rx}^{\rm s}}{\partial z}+\dfrac{\partial v_{rz}^{\rm s}}{\partial x}\right) \end{cases} \tag{8c}$$

which generate the downgoing P-wave source wavefield, reflected P-wave (i.e., PP wave), and converted S-wave (i.e., PS wave), respectively, as displayed in Fig. 1. The three vector waves in (8a)–(8c) are, respectively, denoted as $\begin{bmatrix} v_{0x}^{\rm p} \\ v_{0z}^{\rm p} \end{bmatrix}$, $\begin{bmatrix} v_{rx}^{\rm p} \\ v_{rz}^{\rm p} \end{bmatrix}$, and $\begin{bmatrix} v_{rx}^{\rm s} \\ v_{rz}^{\rm s} \end{bmatrix}$. The subscript of zero indicates that elastic moduli are converted from smoothed migration velocity models.

The wave equations in (8) are obtained by simplifying (B-4)–(B-6) under the assumption that P- and S-wave stresses are only related to their respective particle velocities. This assumption is valid only when migration velocity models are sufficiently smoothed and there are no strong conversions of wave modes during wavefield propagations. Equations (8a) and (8b) solve standard acoustic-wave equations, which is a reasonable and stable approximation for P-wave propagation. Equation (8c) is not stable if migration velocity models are not sufficiently smoothed as it neglects the contribution of compressional strain to the shear stress. Therefore, rather than using (8c), we use the following more stable equations to simulate the PS-wave mode:

$$\begin{cases} \rho_0\dfrac{\partial v_{rx}}{\partial t} = \dfrac{\partial \sigma_{rxx}}{\partial x}+\dfrac{\partial \sigma_{rxz}}{\partial z}+R_{\rm ps}(\mathbf{x})v_{0x}^{\rm p} \\ \rho_0\dfrac{\partial v_{rz}}{\partial t} = \dfrac{\partial \sigma_{rxz}}{\partial x}+\dfrac{\partial \sigma_{rzz}}{\partial z}+R_{\rm ps}(\mathbf{x})v_{0z}^{\rm p} \\ \dfrac{\partial \sigma_{rxx}}{\partial t} = (\lambda_0+2\mu_0)\dfrac{\partial v_{rx}}{\partial x}+\lambda_0\dfrac{\partial v_{rz}}{\partial z} \\ \dfrac{\partial \sigma_{rzz}}{\partial t} = \lambda_0\dfrac{\partial v_{rx}}{\partial x}+(\lambda_0+2\mu_0)\dfrac{\partial v_{rz}}{\partial z} \\ \dfrac{\partial \sigma_{rxz}}{\partial t} = \mu_0\left(\dfrac{\partial v_{rx}}{\partial z}+\dfrac{\partial v_{rz}}{\partial x}\right) \end{cases} \tag{9a}$$

and

$$\begin{cases} \rho_0\dfrac{\partial v_{rx}^{\rm p}}{\partial t} = \dfrac{\partial}{\partial x}\dfrac{(\lambda_0+2\mu_0)}{2(\lambda_0+\mu_0)}(\sigma_{rxx}+\sigma_{rzz}) \\ \rho_0\dfrac{\partial v_{rz}^{\rm p}}{\partial t} = \dfrac{\partial}{\partial z}\dfrac{(\lambda_0+2\mu_0)}{2(\lambda_0+\mu_0)}(\sigma_{rxx}+\sigma_{rzz}) \\ v_{rx}^{\rm s} = v_{rx}-v_{rx}^{\rm p} \\ v_{rz}^{\rm s} = v_{rz}-v_{rz}^{\rm p}. \end{cases} \tag{9b}$$

### D. VERTM for Gradient

We numerically implement the adjoint migration operator with the decoupled velocity–stress equations. In the first step, we propagate the source wavefieds by solving the following equations in the forward time:

$$\begin{cases} \rho_0\dfrac{\partial v_{0x}}{\partial t} = \dfrac{\partial \sigma_{0xx}}{\partial x}+\dfrac{\partial \sigma_{0xz}}{\partial z} \\ \rho_0\dfrac{\partial v_{0z}}{\partial t} = \dfrac{\partial \sigma_{0xz}}{\partial x}+\dfrac{\partial \sigma_{0zz}}{\partial z} \\ \dfrac{\partial \sigma_{0xx}}{\partial t} = (\lambda_0+2\mu_0)\dfrac{\partial v_{0x}}{\partial x}+\lambda_0\dfrac{\partial v_{0z}}{\partial z}+f \\ \dfrac{\partial \sigma_{0zz}}{\partial t} = \lambda_0\dfrac{\partial v_{0x}}{\partial x}+(\lambda_0+2\mu_0)\dfrac{\partial v_{0z}}{\partial z}+f \\ \dfrac{\partial \sigma_{0xz}}{\partial t} = \mu_0\left(\dfrac{\partial v_{0x}}{\partial z}+\dfrac{\partial v_{0z}}{\partial x}\right) \end{cases} \tag{10a}$$

where $f$ represents the explosive source, and subscript "0" indicates wavefields propagating in smoothed background models. Then, we obtain the separated P-wave vector $\mathbf{V}_0^{\rm p} = \begin{bmatrix} v_{0x}^{\rm p} \\ v_{0z}^{\rm p} \end{bmatrix}$ using the decoupled formula in (2) at each time step.

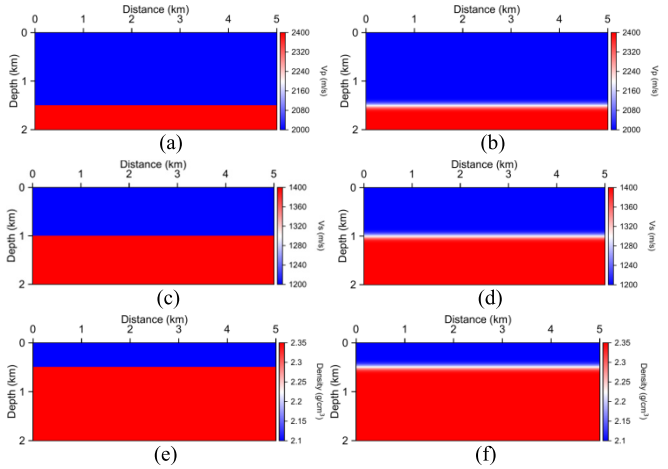


Fig. 2. (a) True and (b) smoothed P-wave velocity model. (c) True and (d) smoothed S-wave velocity model. (e) True and (f) smoothed density model.

In the second step, we solve the following equations in the reverse time to backward propagate the adjoint source:

$$\begin{cases} \rho_0 \dfrac{\partial \tilde{v}_{rx}}{\partial t} = \dfrac{\partial \tilde{\sigma}_{rxx}}{\partial x} + \dfrac{\partial \tilde{\sigma}_{rxz}}{\partial z} + (\mathrm{d}_x - D_x) \\ \rho_0 \dfrac{\partial \tilde{v}_{rz}}{\partial t} = \dfrac{\partial \tilde{\sigma}_{rxz}}{\partial x} + \dfrac{\partial \tilde{\sigma}_{rzz}}{\partial z} + (\mathrm{d}_z - D_z) \\ \dfrac{\partial \tilde{\sigma}_{rxx}}{\partial t} = (\lambda_0 + 2\mu_0)\dfrac{\partial \tilde{v}_{rx}}{\partial x} + \lambda_0 \dfrac{\partial \tilde{v}_{rz}}{\partial z} \\ \dfrac{\partial \tilde{\sigma}_{rzz}}{\partial t} = \lambda_0 \dfrac{\partial \tilde{v}_{rx}}{\partial x} + (\lambda_0 + 2\mu_0)\dfrac{\partial \tilde{v}_{rz}}{\partial z} \\ \dfrac{\partial \tilde{\sigma}_{rxz}}{\partial t} = \mu_0 \left( \dfrac{\partial \tilde{v}_{rx}}{\partial z} + \dfrac{\partial \tilde{v}_{rz}}{\partial x} \right). \end{cases} \tag{10b}$$

At each time step, we decouple the total receiver vector wavefield $\begin{bmatrix} \tilde{v}_{rx} \\ \tilde{v}_{rz} \end{bmatrix}$ into the P-wave vector $\tilde{\mathbf{V}}_{\mathrm{r}}^{\mathrm{p}} = \begin{bmatrix} \tilde{v}_{rx}^{\mathrm{p}} \\ \tilde{v}_{rz}^{\mathrm{p}} \end{bmatrix}$ and the S-wave vector $\tilde{\mathbf{V}}_{\mathrm{r}}^{\mathrm{s}} = \begin{bmatrix} \tilde{v}_{rx}^{\mathrm{s}} \\ \tilde{v}_{rz}^{\mathrm{s}} \end{bmatrix}$ using (2).

In the third step, we produce a gradient with the imaging condition

$$\begin{cases} \tilde{R}_{\mathrm{pp}}(\mathbf{x}) = \displaystyle\int\int \mathbf{V}_0^{\mathrm{p}} \cdot \tilde{\mathbf{V}}_{\mathrm{r}}^{\mathrm{p}} \mathrm{d}t \mathrm{d}\mathbf{x}_{\mathrm{s}} \\ \tilde{R}_{\mathrm{ps}}(\mathbf{x}) = \displaystyle\int\int \mathbf{V}_0^{\mathrm{p}} \cdot \tilde{\mathbf{V}}_{\mathrm{r}}^{\mathrm{s}} \mathrm{d}t \mathrm{d}\mathbf{x}_{\mathrm{s}} \end{cases} \tag{10c}$$

which is different from (7), as solving velocity–stress formulas of (10b) in the reverse time order has implicitly imposed the operation of $-\partial/(\partial t)$ on the adjoint sources in advance.

## III. Numerical Examples

In our synthetic examples, we generate synthetic "observed data" using the true (original, unsmoothed) P-wave velocity, S-wave velocity, and density models, whereas we use only smoothed velocity models (unknown density) [29] for our VELSRTM method to produce PP and PS images.

### A. Layer Model

We first validate our VELSRTM method using a layered model with P-wave, S-wave, and density models shown in Fig. 2. The models are defined on 1001 × 401 grids with a 5-m grid spacing. We generate a total of 41 shot gathers of synthetic data with the true models and a 15-Hz Ricker source wavelet excited at the surface between 1.5 and 3.5 km with a 50-m shot interval. Each shot contains 301 receivers with a split-spread geometry and a 10-m receiver interval.

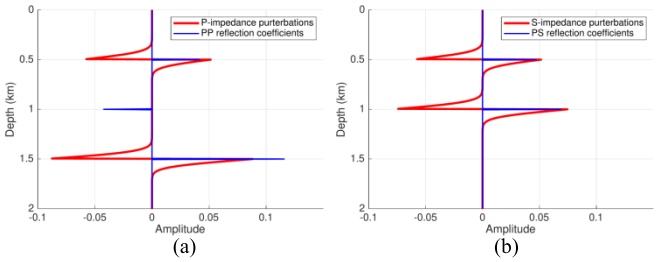


Fig. 3. (a) Theoretical P-impedance perturbations and PP reflection coefficients. (b) Theoretical S-impedance perturbations and PS reflection coefficients.

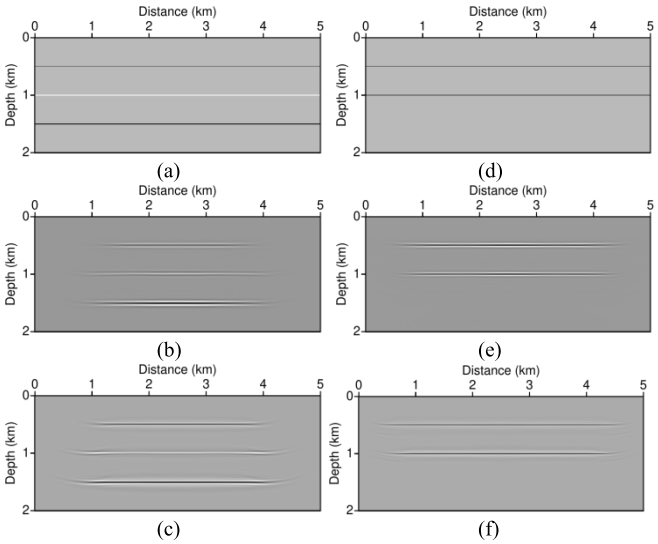


Fig. 4. (a) PP reflectivity model. (b) VERTM and (c) VELSRTM images of PP reflections. (d) PS reflectivity model. (e) VERTM and (f) VELSRTM images of PS reflections.

We calculate theoretical PP and PS reflection coefficients along depth in this model using the method of Aki and Richards [30], as shown in Fig. 3. These results provide a reference for our VELSRTM PP and PS images. Fig. 3 also displays the impedance perturbations for comparison. The P-wave velocity, S-wave velocity, and density variations with depth all contribute to PP reflections, while only the S-wave velocity and density variations with depth contribute to the PS reflections, as suggested by the scattering radiation patterns of elastic waves [31].

With smoothed migration velocity models, we generate the VERTM and VELSRTM images of PP and PS reflections, as displayed in Fig. 4. Both PP and PS images contain consistent layer positions with theoretical reflectivity models. We find that our VELSRTM method improves PP and PS images with more balanced amplitudes and higher resolution compared with those of the conventional VERTM images.

We show snapshots at the one-second time step in Fig. 5. Comparing four figures in the left column, we find that

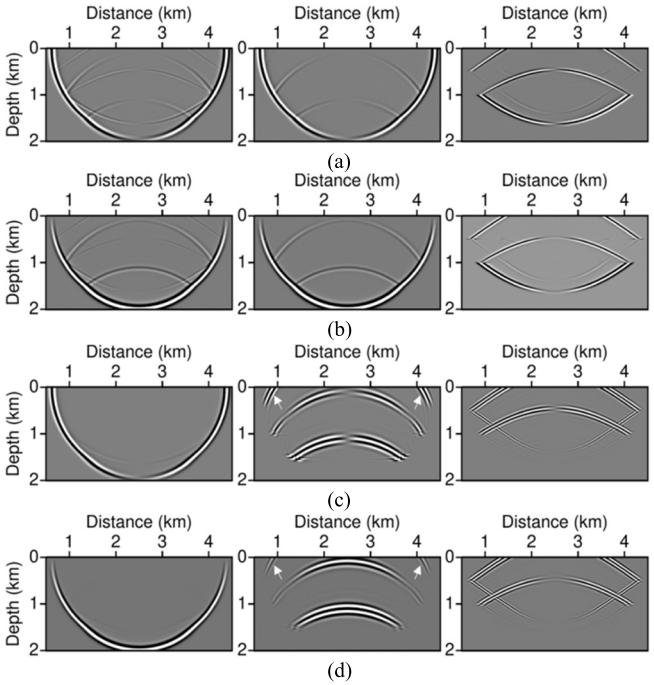


Fig. 5. (a) and (b) Horizontal and vertical wavefield components obtained using elastic forward modeling in the true models, respectively, where the standard wavefields and the decoupled P- and S-wave modes are displayed in the left, middle, and right columns, respectively. (c) and (d) Horizontal and vertical components obtained using demigration in the smoothed migration velocity models, where the downgoing wavefields and the PP and PS wavefields are, respectively, depicted in the left, middle, and right columns.

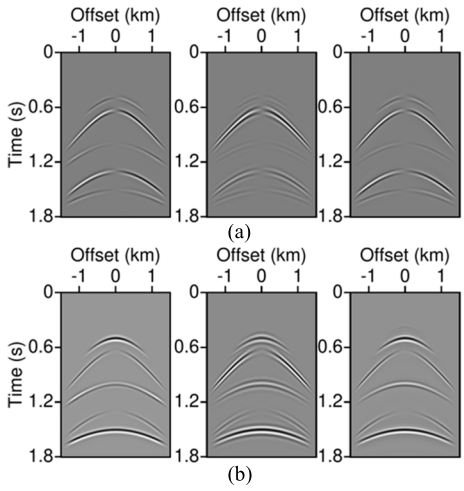


Fig. 6. (a) Horizontal and (b) vertical components of seismic data, where the observed data and the demigration data at the first and fifth iterations are, respectively, shown in the left, middle, and right columns. The demigration data become much closer to the observed data after five iterations.

most reflected and converted wavefields vanish on smoothed velocity models. Demigration wavefields in Fig. 5(c) and (d) are reflected by initial stacked VERTM images and contain low-resolution seismic events. As indicated by the arrowed lines, we observe that the demigration waves have stronger amplitudes at far offsets compared with those in Figs. 5(a) and 6(b). The reason is that the demigration procedure with stacked images annihilates the angle information and loses some accuracy to save computational cost as discussed in

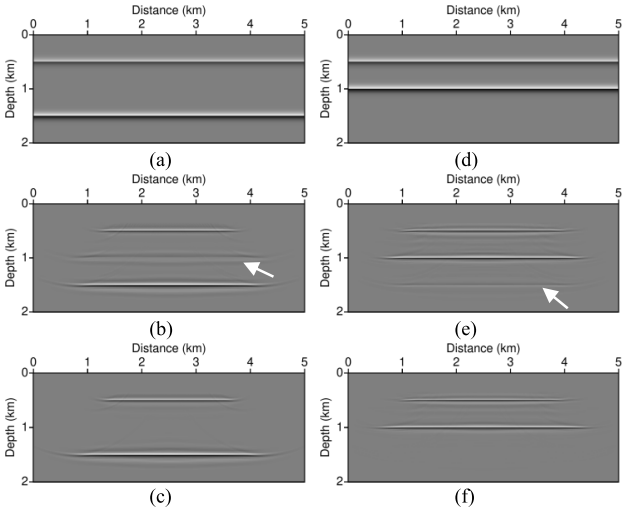


Fig. 7. (a) P-wave impedance (PI) perturbations and ELSRTM images of PI perturbations: (b) without and (c) with elastic-wave decoupling. (d) S-wave impedance (SI) perturbations and ELSRTM images of SI perturbations: (e) without and (f) with elastic-wave decoupling.

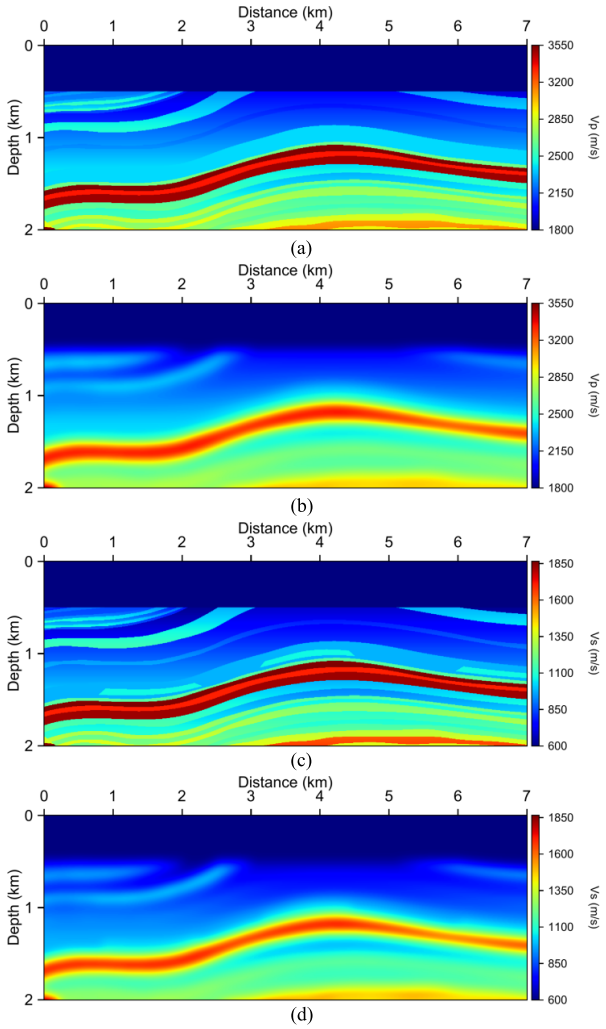


Fig. 8. (a) True and (b) smoothed P-wave velocity models of a modified Marmousi2 model. The corresponding (c) true and (d) smoothed S-wave velocity models.

Appendix C. Furthermore, we compare the horizontal and vertical components of demigration data with those of observed data in Fig. 6(a) and (b), respectively. The demigration data

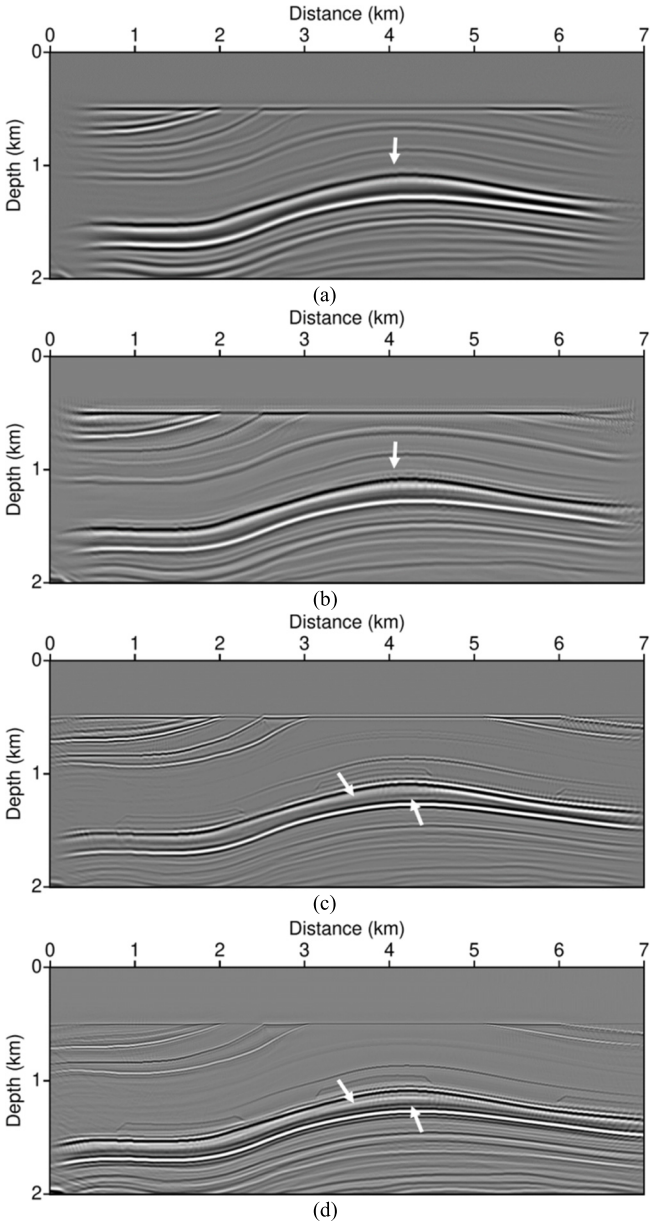


Fig. 9. (a) VERTM and (b) VELSRTM PP images and (c) VERTM and (d) VELSRTM PS images for the modified Marmousi2 model. VELSRTM improves reflectivity images by increasing the image resolution as indicated by the arrows and balancing the image amplitudes.

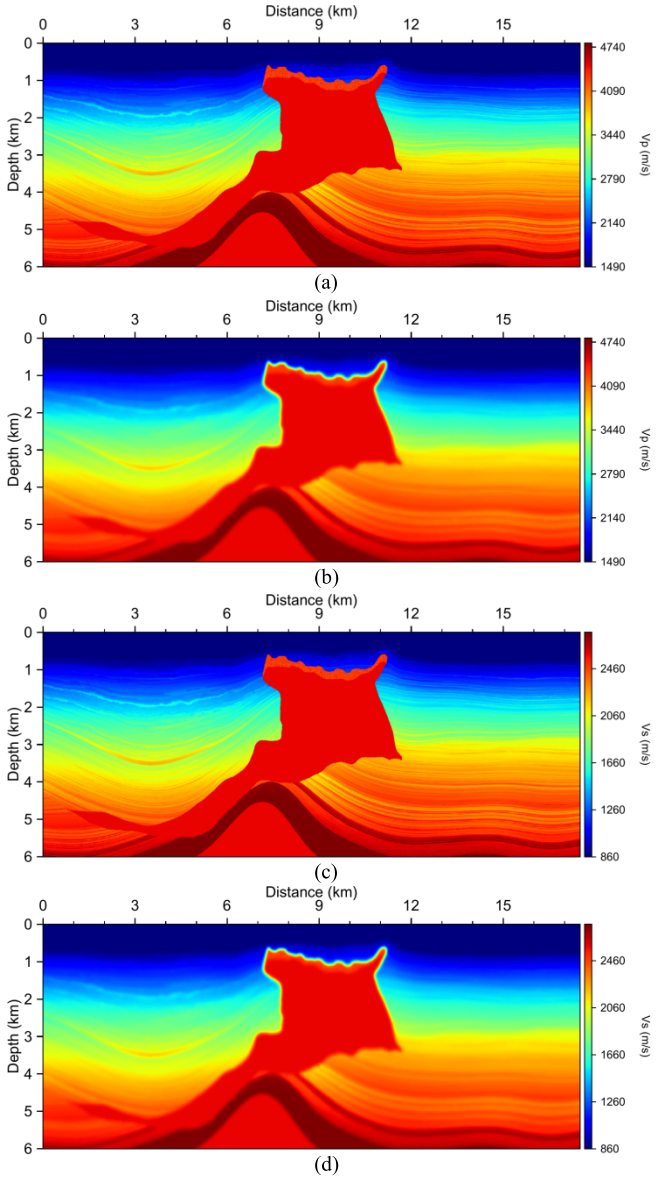


Fig. 10. (a) True and (b) smoothed P-wave velocity models of an SEG Advanced Modeling (SEAM) model. The corresponding (c) true and (d) smoothed S-wave velocity models.

show more focused events and match better with the observed data after five iterations.

For reference, we also produce P- and S-impedance perturbation images without and with decoupled elastic wave equations [32], as shown in Fig. 7. The results obtained using decoupled wave equations mitigate most of the interparameter cross-talks and produce imaging events consistent with theoretical impedance perturbation models. Comparing with Fig. 4, we observe that PP reflectivity image contains contributions from S-wave velocity perturbations while P-impedance perturbation image does not, and that perturbation images have a phase rotation relative to zero phase reflectivity images.

### *B. Marmousi2 Model*

We modify the top-right region of the Marmousi2 models for our next numerical example. Fig. 8 displays the true models and the smoothed migration velocity models defined on 1401 × 401 grids with a 5-m grid spacing. We generate a total of 141 synthetic shot gathers using the true models and a 15-Hz Ricker source wavelet excited at the surface between 0.7 and 6.3 km with a 40-m shot interval. Each shot contains 281 receivers with a split-spread geometry and a 10-m receiver interval.

We use the smoothed P-wave and S-wave migration velocity models, as shown in Fig. 8(b) and (d), respectively, for migration. We display VERTM and our VELSRTM PP images in Fig. 9(a) and (b), respectively. We show the corresponding PS images in Fig. 9(c) and (d). Our VELSRTM improves the imaging resolution and balances the image amplitudes. For instance, as indicated by the arrows in Fig. 9(a) and (b), a weak event that is blurred in the VERTM PP image is clearly imaged in our VELSRTM PP image. In general, PS images have higher resolution than corresponding PP images, and the sand structures with zero P-impedance [33] can only be detected by PS images in this numerical example. Our VELSRTM method

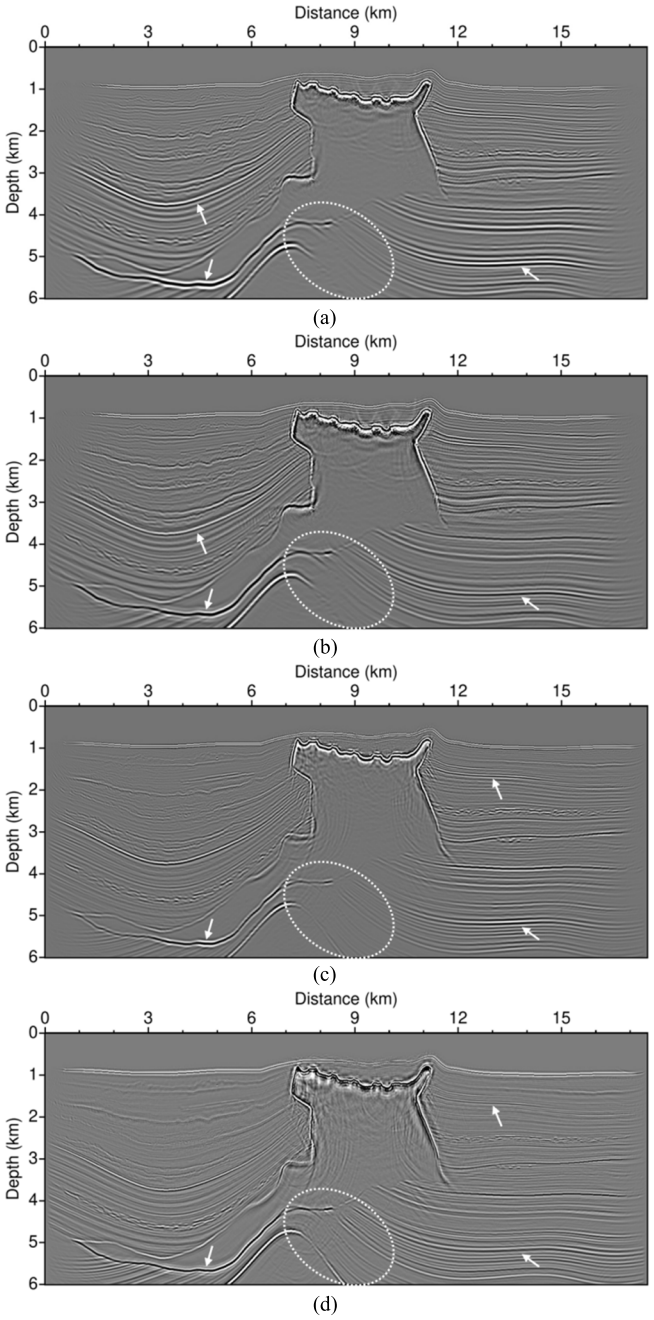


Fig. 11. (a) VERTM and (b) VELSRTM PP images and (c) VERTM and (d) VELSRTM PS images for the SEAM model. VELSRTM enhances the imaging resolution with better focused events as indicated by the arrows and balances image amplitudes as indicated by the ellipses.

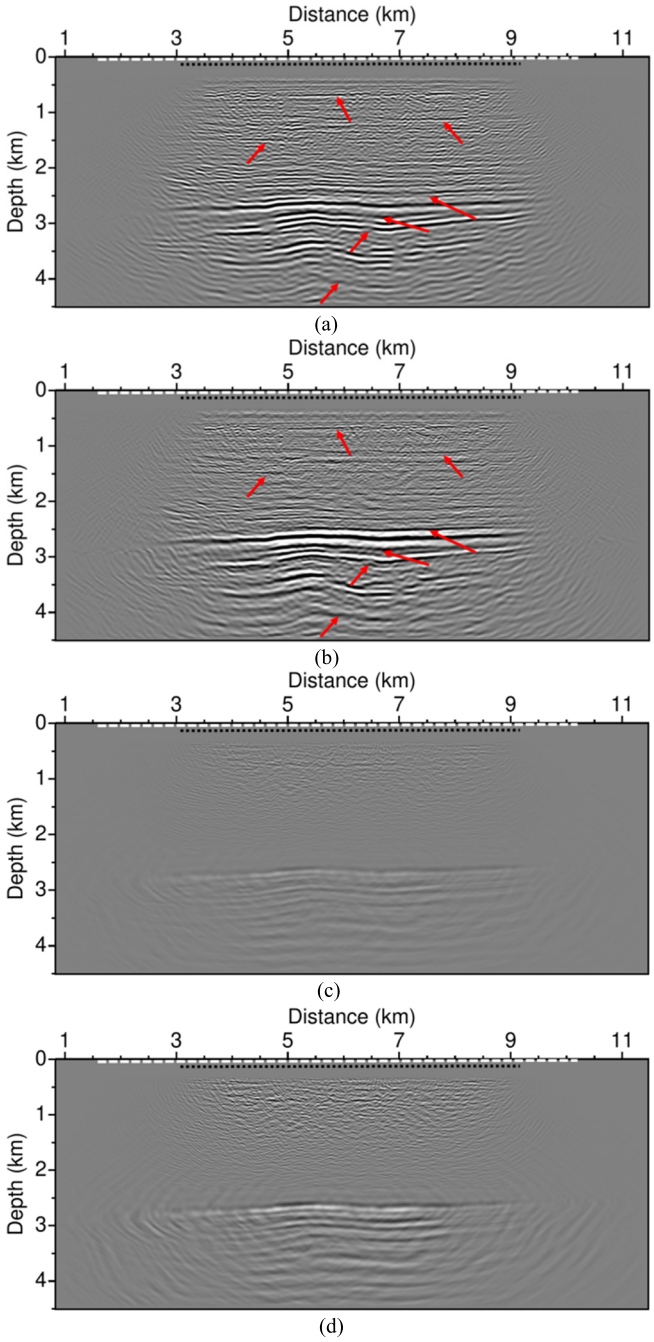


Fig. 12. (a) VERTM and (b) VELSRTM PP images and (c) VERTM and (d) VELSRTM PS images, where source and receiver positions are indicated by the white dashed line and the black dotted line, respectively. Image improvements are indicated by the red arrows.

further increases the imaging resolution of the PS image. As indicated by the arrows in Fig. 9(c) and (d), two interfaces, corresponding to a small layer inside the high-velocity body in the true models, can be more clearly imaged using our VELSRTM method. Our method does not have the crosstalk issue. We use only seven iterations to significantly improve the image quality. Additional iterations do not provide meaningful image improvement while increasing computational cost.

### C. SEAM Salt Model

We also test our VELSRTM method using the SEAM model. Fig. 10 shows the true and smoothed velocity models discretized on 1751 $\times$ 601 grids with a 10-m grid spacing. We generate a total of 281 synthetic shot gathers using the true models and a 15-Hz Ricker source wavelet excited at the surface between 2 and 16 km with a 50-m shot interval. Each shot contains 801 receivers with a split-spread geometry and a 10-m receiver interval.

Using the smoothed migration velocity models, we obtain the VERTM and VELSRTM PP images in Fig. 11(a) and (b), respectively, and the corresponding PS images in Fig. 11(c) and (d), respectively. Our VELSRTM method with seven iterations improves the image resolution with better focused events

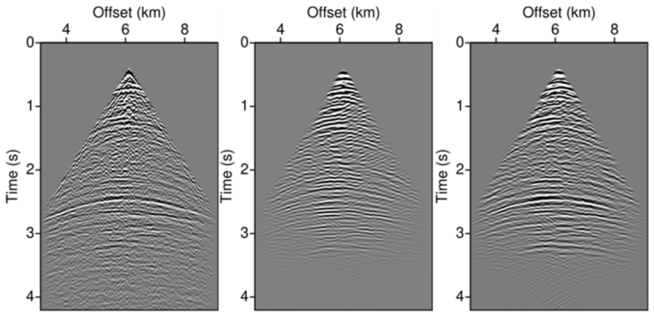


Fig. 13. Observed data and the demigration data at the first and fifth iterations are, respectively, shown in the left, middle, and right columns. We use the preprocessed PP data as the vertical-component observed data.

as indicated by the arrows and balances image amplitudes as indicated by the ellipses. As shown within the area enclosed by the ellipses, PS images can better delineate subsalt structure than PP images, similar to observations by Stewart et al. [2]. The reason is that the limited-aperture receiver array cannot record subsalt PP waves with large reflection angles while it can record PS waves with relatively smaller reflection angles, as depicted in Fig. 1.

### D. Volve OBC Data

We verified our VELSRTM method using the Volve Ocean Bottom Cable (OBC) field dataset. The source and receiver positions are indicated with the white dashed line and the black dotted line in Fig. 12, respectively. We follow Duan et al. [20] to set the preprocessed PP data as the vertical component except using a higher maximum frequency of 30 Hz. Duan et al. [20] produced images of P- and S-wave velocity perturbations, whereas our VELSRTM mainly outputs PP images. As shown in Fig. 12, our method successfully improves the image resolution with more focused reflectors, as indicated by the red arrows, balances the image amplitudes, and suppresses image noise. We also produce PS images but they show low amplitude and low quality, which might result from some secondary elastic-wave conversions in the deep subsurface. The modeled data iteratively become closer to the observed data, as shown in Fig. 13. Even though it is not a perfect example, it demonstrates that our method improves migration images even using single-component seismic data.

## IV. Conclusion

We have developed a novel VELSRTM for directly migrating elastic seismic data to produce PP and PS reflectivity images. Our VELSRTM method employs a novel vector reflection demigration operator based on the reflection demigration theory. For numerical implementation, we have solved the simplified decoupling velocity–stress equations to achieve the demigration modeling of PP and PS waves. We have demonstrated using synthetic and field seismic data that our VELSRTM method improves the imaging quality with higher resolution and more balanced image amplitudes with only a few iterations.

## Appendix A
## Elastic-Wave Equations for Displacement and Particle Velocity With Curl- and Divergence-Free Terms

The equation of motion in isotropic media can be fully represented with displacements after replacing stresses with strains based on the constitutive equation. Taking $x$-direction as an example, it is written as

$$\rho\frac{\partial^2 u_x}{\partial t^2} = \frac{\partial}{\partial x}(\lambda+2\mu)\left(\frac{\partial u_x}{\partial x}+\frac{\partial u_y}{\partial y}+\frac{\partial u_z}{\partial z}\right) - 2\frac{\partial}{\partial x}\mu\left(\frac{\partial u_y}{\partial y}+\frac{\partial u_z}{\partial z}\right) + \frac{\partial}{\partial y}\mu\left(\frac{\partial u_x}{\partial y}+\frac{\partial u_y}{\partial x}\right)+\frac{\partial}{\partial z}\mu\left(\frac{\partial u_x}{\partial z}+\frac{\partial u_z}{\partial x}\right). \tag{A-1}$$

If the shear modulus $\mu$ is homogeneous or at least locally smooth, we can rewrite (A-1) as

$$\rho\frac{\partial^2 u_x}{\partial t^2} = \frac{\partial}{\partial x}(\lambda+2\mu)\left(\frac{\partial u_x}{\partial x}+\frac{\partial u_y}{\partial y}+\frac{\partial u_z}{\partial z}\right) + \frac{\partial}{\partial y}\mu\left(\frac{\partial u_x}{\partial y}-\frac{\partial u_y}{\partial x}\right)+\frac{\partial}{\partial z}\mu\left(\frac{\partial u_x}{\partial z}-\frac{\partial u_z}{\partial x}\right). \tag{A-2}$$

Considering all wavefield components and inserting an external source, the elastic-wave equation can be compactly written as

$$\rho\frac{\partial^2 \mathbf{U}}{\partial t^2} = \nabla(\lambda+2\mu)\nabla\cdot\mathbf{U} - \nabla\times\mu\nabla\times\mathbf{U}+\mathbf{F} \tag{A-3}$$

where $\mathbf{U}$ and $\mathbf{F}$ represent the displacement vector and the source term, respectively. The right-hand side of (A-3) contains a curl-free term and a divergence-free term.

Equation (A-3) can be written for particle velocity by applying a time derivative

$$\rho\frac{\partial^2 \mathbf{V}}{\partial t^2} = \nabla(\lambda+2\mu)\nabla\cdot\mathbf{V} - \nabla\times\mu\nabla\times\mathbf{V}+\frac{\partial\mathbf{F}}{\partial t} \tag{A-4}$$

where $\mathbf{V}$ represents the particle-velocity vector.

On the other hand, equivalent to (A-4), the velocity–stress formulas [28] are written as

$$\frac{\partial\boldsymbol{\sigma}}{\partial t} = \mathbf{CHV} \tag{A-5}$$

$$\rho\frac{\partial\mathbf{V}}{\partial t} = \mathbf{H}^{\mathrm{T}}\boldsymbol{\sigma}+\mathbf{F} \tag{A-6}$$

where $\boldsymbol{\sigma}$, $\mathbf{C}$, and $\mathbf{H}$ compactly represent the stress tensor, the stiffness matrix, and the matrix of differential operators, respectively. Relative to (A-4), solving (A-5) and (A-6) implicitly applies a first-order time-derivative operation to the source term.

## Appendix B
## Decomposing Constitutive Relations for Decoupled P- and S-Wave

We can directly split standard velocity–stress equations [28] to obtain decoupled P- and S-wave equations by decomposing

the constitutive relations. In the 2-D space, we first write the expressions of stresses as

$$\begin{cases} \dfrac{\partial \sigma_{xx}}{\partial t} = (\lambda + 2\mu)\left(\dfrac{\partial v_x}{\partial x} + \dfrac{\partial v_z}{\partial z}\right) - 2\mu \dfrac{\partial v_z}{\partial z} \\ \dfrac{\partial \sigma_{zz}}{\partial t} = (\lambda + 2\mu)\left(\dfrac{\partial v_x}{\partial x} + \dfrac{\partial v_z}{\partial z}\right) - 2\mu \dfrac{\partial v_x}{\partial x} \\ \dfrac{\partial \sigma_{xz}}{\partial t} = \mu\left(\dfrac{\partial v_x}{\partial z} + \dfrac{\partial v_z}{\partial x}\right) \end{cases} \tag{B-1}$$

and then directly decompose them into P- and S-wave parts

$$\frac{\partial \sigma^{\mathrm{p}}}{\partial t} = \frac{\partial \sigma^{\mathrm{p}}_{xx}}{\partial t} = \frac{\partial \sigma^{\mathrm{p}}_{zz}}{\partial t} = (\lambda + 2\mu)\left(\frac{\partial v_x}{\partial x} + \frac{\partial v_z}{\partial z}\right) \tag{B-2}$$

and

$$\begin{cases} \dfrac{\partial \sigma^{\mathrm{s}}_{xx}}{\partial t} = -2\mu \dfrac{\partial v_z}{\partial z} \\ \dfrac{\partial \sigma^{\mathrm{s}}_{zz}}{\partial t} = -2\mu \dfrac{\partial v_x}{\partial x} \\ \dfrac{\partial \sigma^{\mathrm{s}}_{xz}}{\partial t} = \mu\left(\dfrac{\partial v_x}{\partial z} + \dfrac{\partial v_z}{\partial x}\right) \end{cases} \tag{B-3}$$

where the first part is for propagation of the P-wave wavefield and the second part is propagation of the S-wave wavefield.

Therefore, the complete separated velocity–stress formulas for P- and S-waves are written as

$$\begin{cases} \rho \dfrac{\partial v^{\mathrm{p}}_x}{\partial t} = \dfrac{\partial \sigma^{\mathrm{p}}}{\partial x} \\ \rho \dfrac{\partial v^{\mathrm{p}}_z}{\partial t} = \dfrac{\partial \sigma^{\mathrm{p}}}{\partial z} \\ \dfrac{\partial \sigma^{\mathrm{p}}}{\partial t} = (\lambda + 2\mu)\left(\dfrac{\partial v_x}{\partial x} + \dfrac{\partial v_z}{\partial z}\right) \end{cases} \tag{B-4}$$

$$\begin{cases} \rho \dfrac{\partial v^{\mathrm{s}}_x}{\partial t} = \dfrac{\partial \sigma^{\mathrm{s}}_{xx}}{\partial x} + \dfrac{\partial \sigma^{\mathrm{s}}_{xz}}{\partial z} \\ \rho \dfrac{\partial v^{\mathrm{s}}_z}{\partial t} = \dfrac{\partial \sigma^{\mathrm{s}}_{xz}}{\partial x} + \dfrac{\partial \sigma^{\mathrm{s}}_{zz}}{\partial z} \\ \dfrac{\partial \sigma^{\mathrm{s}}_{xx}}{\partial t} = -2\mu \dfrac{\partial v_z}{\partial z} \\ \dfrac{\partial \sigma^{\mathrm{s}}_{zz}}{\partial t} = -2\mu \dfrac{\partial v_x}{\partial x} \\ \dfrac{\partial \sigma^{\mathrm{s}}_{xz}}{\partial t} = \mu\left(\dfrac{\partial v_x}{\partial z} + \dfrac{\partial v_z}{\partial x}\right) \end{cases} \tag{B-5}$$

and

$$\begin{cases} v_x = v^{\mathrm{p}}_x + v^{\mathrm{s}}_x \\ v_z = v^{\mathrm{p}}_z + v^{\mathrm{s}}_z. \end{cases} \tag{B-6}$$

We can further rewrite (B-4)–(B-6) to connect with (1) based on the Helmholtz decomposition. We first rewrite (B-4) by replacing stresses in its first and second formulas with its third formula as

$$\begin{cases} \rho \dfrac{\partial^2 v^{\mathrm{p}}_x}{\partial t^2} = \dfrac{\partial}{\partial x}(\lambda + 2\mu)\left(\dfrac{\partial v_x}{\partial x} + \dfrac{\partial v_z}{\partial z}\right) \\ \rho \dfrac{\partial^2 v^{\mathrm{p}}_z}{\partial t^2} = \dfrac{\partial}{\partial z}(\lambda + 2\mu)\left(\dfrac{\partial v_x}{\partial x} + \dfrac{\partial v_z}{\partial z}\right). \end{cases} \tag{B-7}$$

Similarly, we can rewrite (B-5) as

$$\begin{cases} \rho \dfrac{\partial^2 v^{\mathrm{s}}_x}{\partial t^2} = -2\dfrac{\partial}{\partial x}\mu \dfrac{\partial v_z}{\partial z} + \dfrac{\partial}{\partial z}\mu\left(\dfrac{\partial v_x}{\partial z} + \dfrac{\partial v_z}{\partial x}\right) \\ \rho \dfrac{\partial^2 v^{\mathrm{s}}_z}{\partial t^2} = \dfrac{\partial}{\partial x}\mu\left(\dfrac{\partial v_x}{\partial z} + \dfrac{\partial v_z}{\partial x}\right) - 2\dfrac{\partial}{\partial z}\mu \dfrac{\partial v_x}{\partial x}. \end{cases} \tag{B-8}$$

Furthermore, by assuming the shear modulus is homogeneous or at least locally smooth, we simplify (B-8) as

$$\begin{cases} \rho \dfrac{\partial^2 v^{\mathrm{s}}_x}{\partial t^2} = \dfrac{\partial}{\partial z}\mu\left(\dfrac{\partial v_x}{\partial z} - \dfrac{\partial v_z}{\partial x}\right) \\ \rho \dfrac{\partial^2 v^{\mathrm{s}}_z}{\partial t^2} = \dfrac{\partial}{\partial x}\mu\left(\dfrac{\partial v_z}{\partial x} - \dfrac{\partial v_x}{\partial z}\right). \end{cases} \tag{B-9}$$

In the 2-D space, the time integral of (B-7) and that of (B-9) are equivalent to (1a) and (1b), respectively.

## Appendix C
## Reflection Demigration Formulas in the Frequency Domain

Starting from acoustic media, the incident wavefield $P_0$ and the scattered/reflected wavefield $P_{\mathrm{r}}$ can be related using an angle-dependent reflectivity function [25]

$$R(\mathbf{x}, \theta) = \frac{P_{\mathrm{r}}(\mathbf{x}, \omega; \mathbf{x}_{\mathrm{s}})}{P_0(\mathbf{x}, \omega; \mathbf{x}_{\mathrm{s}})} \tag{C-1}$$

$$\frac{\partial P_{\mathrm{r}}(\mathbf{x}, \omega; \mathbf{x}_{\mathrm{s}})}{\partial \mathbf{n}} = -R(\mathbf{x}, \theta)\frac{\partial P_0(\mathbf{x}, \omega; \mathbf{x}_{\mathrm{s}})}{\partial \mathbf{n}} \tag{C-2}$$

where $\theta$ represents the incident angle, $\omega$ represents the circular frequency, and $\mathbf{n}$ represents the upward normal vector at the local reflector position of $\mathbf{x}$, as illustrated in Fig. 1. By expanding wavefields in (C-1) and (C-2) with Green's functions, the recorded reflection data $\mathrm{d}_{\mathrm{R}}(\mathbf{x}_{\mathrm{r}}, \omega; \mathbf{x}_{\mathrm{s}})$ can be represented with the integral formula [25]

$$\begin{aligned} &\mathrm{d}_{\mathrm{R}}(\mathbf{x}_{\mathrm{r}}, \omega; \mathbf{x}_{\mathrm{s}}) \\ &= \int R(\mathbf{x}, \theta)\left(\begin{array}{l} G_0(\mathbf{x}, \omega; \mathbf{x}_{\mathrm{s}})\dfrac{\partial G_0(\mathbf{x}_{\mathrm{r}}, \omega; \mathbf{x})}{\partial \mathbf{n}} \\ \quad + G_0(\mathbf{x}_{\mathrm{r}}, \omega; \mathbf{x})\dfrac{\partial G_0(\mathbf{x}, \omega; \mathbf{x}_{\mathrm{s}})}{\partial \mathbf{n}} \end{array}\right) f(\omega; \mathbf{x}_{\mathrm{s}})\mathrm{d}\mathbf{x} \end{aligned} \tag{C-3}$$

where $f(\omega; \mathbf{x}_{\mathrm{s}})$ represents the source function, and $G_0$ denotes Green's functions in a smoothed background model. The formula is first accurately established for the single-reflector case and is further approximately extended to the general subsurface with the assumption of single primary reflections.

After replacing normal gradients with high-frequency asymptotic solutions [25], (C-3) can be approximately simplified as

$$\begin{aligned} &\mathrm{d}_{\mathrm{R}}(\mathbf{x}_{\mathrm{r}}, \omega; \mathbf{x}_{\mathrm{s}}) \\ &= i\omega f(\omega; \mathbf{x}_{\mathrm{s}}) \\ &\quad \times \int \frac{2\cos(\theta)}{V_{\mathrm{p}}(\mathbf{x})} G_0(\mathbf{x}_{\mathrm{r}}, \omega; \mathbf{x}) R(\mathbf{x}, \theta) G_0(\mathbf{x}, \omega; \mathbf{x}_{\mathrm{s}})\mathrm{d}\mathbf{x} \end{aligned} \tag{C-4}$$

where $V_{\mathrm{p}}$ denotes the P-wave velocity, and $\theta$ represents the incident angle at any subsurface point.

Neglecting angle-dependent information, (C-4) can be simplified for more efficient computation as follows:

$$\begin{aligned} &\mathrm{d}_{\mathrm{R}}(\mathbf{x}_{\mathrm{r}}, \omega; \mathbf{x}_{\mathrm{s}}) \\ &\quad \approx i\omega \int G_0(\mathbf{x}_{\mathrm{r}}, \omega; \mathbf{x}) R(\mathbf{x}) G_0(\mathbf{x}, \omega; \mathbf{x}_{\mathrm{s}}) f(\mathbf{x}_{\mathrm{s}}, \omega)\mathrm{d}\mathbf{x} \end{aligned} \tag{C-5}$$

where $R(\mathbf{x})$ represents a stacked reflectivity model. Its adjoint operator denotes a standard migration operator, which produces a stacked image $\tilde{R}(\mathbf{x})$

$$\tilde{R}(\mathbf{x}) = \int\int\int \mathrm{d}\omega \mathrm{d}\mathbf{x}_\mathrm{r} \mathrm{d}\mathbf{x}_\mathrm{s} \times -i\omega(G_0(\mathbf{x}, \omega; \mathbf{x}_\mathrm{s}) f(\mathbf{x}_\mathrm{s}, \omega))^* G_0^*(\mathbf{x}_\mathrm{r}, \omega; \mathbf{x}) \mathrm{d}_\mathrm{R} \times (\mathbf{x}_\mathrm{r}, \omega; \mathbf{x}_\mathrm{s}). \tag{C-6}$$

## ACKNOWLEDGMENT

This article used resources provided by the Los Alamos National Laboratory (LANL) Institutional Computing Program.

## REFERENCES

[1] J. Etgen, S. H. Gray, and Y. Zhang, "An overview of depth imaging in exploration geophysics," *Geophysics*, vol. 74, no. 6, pp. 5–17, 2009, doi: 10.1190/1.3223188.

[2] R. R. Stewart, J. E. Gaiser, R. J. Brown, and D. C. Lawton, "Converted-wave seismic exploration: Applications," *Geophysics*, vol. 68, no. 1, pp. 40–57, Jan. 2003.

[3] J. Yan and P. Sava, "Isotropic angle-domain elastic reverse-time migration," *Geophysics*, vol. 73, no. 6, pp. 229–239, 2008.

[4] W. Wang and G. A. McMechan, "Vector-based elastic reverse time migration," *Geophysics*, vol. 80, no. 6, pp. 245–258, 2015.

[5] Q. Du, C. Guo, Q. Zhao, X. Gong, C. Wang, and X. Li, "Vector-based elastic reverse time migration based on scalar imaging condition," *Geophysics*, vol. 82, no. 2, pp. 111–127, 2017.

[6] H. Zhu, "Elastic wavefield separation based on the Helmholtz decomposition," *Geophysics*, vol. 82, no. 2, pp. S173–S183, Mar. 2017.

[7] J. Yang, H. Zhu, W. Wang, Y. Zhao, and H. Zhang, "Isotropic elastic reverse time migration using the phase- and amplitude-corrected vector P- and S-wavefields," *Geophysics*, vol. 83, no. 6, pp. S489–S503, Nov. 2018.

[8] J. Yang, H. Zhang, Y. Zhao, and H. Zhu, "Elastic wavefield separation in anisotropic media based on eigenform analysis and its application in reverse-time migration," *Geophys. J. Int.*, vol. 217, no. 2, pp. 1290–1313, May 2019.

[9] X. Xiao and W. S. Leaney, "Local vertical seismic profiling (VSP) elastic reverse-time migration and migration resolution: Salt-flank imaging with transmitted P-to-S waves," *Geophysics*, vol. 75, no. 2, pp. 35–49, 2010.

[10] T. Nemeth, C. Wu, and G. T. Schuster, "Least-squares migration of incomplete reflection data," *Geophysics*, vol. 64, no. 1, pp. 208–221, Jan. 1999, doi: 10.1190/1.1444517.

[11] Y. Huang, G. Dutta, W. Dai, X. Wang, G. T. Schuster, and J. Yu, "Making the most out of least-squares migration," *Lead. Edge*, vol. 33, no. 9, pp. 954–960, Sep. 2014.

[12] Y. Liu, X. Chang, D. Jin, R. He, H. Sun, and Y. Zheng, "Reverse time migration of multiples for subsalt imaging," *Geophysics*, vol. 76, no. 5, pp. WB209–WB216, Sep. 2011.

[13] Y. Liu, X. Liu, A. Osen, Y. Shao, H. Hu, and Y. Zheng, "Least-squares reverse time migration using controlled-order multiple reflections," *Geophysics*, vol. 81, no. 5, pp. 347–357, 2016.

[14] X. Liu, Y. Liu, H. Lu, H. Hu, and M. Khan, "Prestack correlative least-squares reverse time migration," *Geophysics*, vol. 82, no. 2, pp. 159–172, 2017.

[15] X. Liu, Y. Liu, and M. Khan, "Fast least-squares reverse time migration of VSP free-surface multiples with dynamic phase-encoding schemes," *Geophysics*, vol. 83, no. 4, pp. 321–332, 2018.

[16] Q. Liu, Y. Lu, and H. Zhang, "Fast single-step least-squares reverse-time imaging via adaptive matching filters in beams," *IEEE Trans. Geosci. Remote Sens.*, vol. 58, no. 3, pp. 1913–1919, Mar. 2020.

[17] Y. Liu, J. Teng, T. Xu, Z. Bai, H. Lan, and J. Badal, "An efficient step-length formula for correlative least-squares reverse time migration," *Geophysics*, vol. 81, no. 4, pp. 221–238, 2016.

[18] Y. Hu et al., "A 2-D local correlative misfit for least-squares reverse time migration with sparsity promotion," *IEEE Trans. Geosci. Remote Sens.*, vol. 60, 2022, Art. no. 5911913.

[19] Y. Zhang, Y. Liu, J. Yi, and X. Liu, "Fast least-squares reverse time migration of OBN down-going multiples," *Frontiers Earth Sci.*, vol. 9, p. 827, Sep. 2021.

[20] Y. Duan, A. Guitton, and P. Sava, "Elastic least-squares reverse time migration," *Geophysics*, vol. 82, no. 4, pp. 315–325, 2017.

[21] Z. Feng and G. T. Schuster, "Elastic least-squares reverse time migration," *Geophysics*, vol. 82, no. 2, pp. 143–157, 2017.

[22] Q. Guo and T. Alkhalifah, "Elastic reflection-based waveform inversion with a nonlinear approach," *Geophysics*, vol. 82, no. 6, pp. 309–321, 2017, doi: 10.1190/geo2016-0407.1.

[23] J. Yang, H. Zhu, G. Mcmechan, H. Zhang, and Y. Zhao, "Elastic least-squares reverse time migration in vertical transverse isotropic media," *Geophysics*, vol. 84, no. 6, pp. S539–S553, Nov. 2019.

[24] D. Rocha and P. Sava, "Elastic least-squares reverse time migration using the energy norm," *Geophysics*, vol. 83, no. 3, pp. S237–S248, May 2018.

[25] N. Bleistein, Y. Zhang, S. Xu, G. Zhang, and S. H. Gray, "Migration/inversion: Think image point coordinates, process in acquisition surface coordinates," *Inverse Problems*, vol. 21, no. 5, pp. 1715–1744, Oct. 2005, doi: 10.1088/0266-5611/21/5/013.

[26] Y. Zhang, L. Duan, and Y. Xie, "A stable and practical implementation of least-squares reverse time migration," *Geophysics*, vol. 80, no. 1, pp. 23–31, 2015.

[27] X. Liu and L. Huang, "Vector elastic least-squares reverse-time migration for reflectivity imaging," in *Proc. SEG/AAPG/SEPM 1st Int. Meeting Appl. Geosci. Energy Expanded Abstr.*, Sep. 2021, Art. no. D011S116R002.

[28] J. Virieux, "P-SV wave propagation in heterogeneous media: Velocity-stress finite-difference method," *Geophysics*, vol. 51, no. 4, pp. 889–901, Apr. 1986.

[29] X. Liu, L. Huang, Z. Feng, G. El-kaseeh, R. Will, and R. Balch, "Efficient 3-D velocity model building using joint inline and crossline plane-wave wave-equation migration velocity analyses," *Geophys. J. Int.*, vol. 225, no. 1, pp. 37–53, 2021.

[30] K. Aki and P. G. Richards, *Quantitative Seismology: Theory and Methods*. Madison Ave, NY, USA: W. H. Freeman & Co, 1980.

[31] R. Wu and K. Aki, "Scattering characteristics of elastic waves by an elastic heterogeneity," *Geophysics*, vol. 50, no. 4, pp. 582–595, Apr. 1985.

[32] Y. Qu, J. Li, J. Huang, and Z. Li, "Elastic least-squares reverse time migration with velocities and density perturbation," *Geophys. J. Int.*, vol. 212, no. 2, pp. 1033–1056, Feb. 2018.

[33] G. S. Martin, R. Wiley, and K. J. Marfurt, "Marmousi2: An elastic upgrade for marmousi," *Lead. Edge*, vol. 25, no. 2, pp. 156–166, Feb. 2006.